

Spatial Interactions in Hydrogenated Perovskite Nickelate Synaptic Networks

R. Bisht, J. T. Sadowski

To be published in "Nano Letters"

July 2023

Center for Functional Nanomaterials
Brookhaven National Laboratory

U.S. Department of Energy

USDOE Office of Science (SC), Basic Energy Sciences (BES) (SC-22)

Notice: This manuscript has been authored by employees of Brookhaven Science Associates, LLC under Contract No. DE-SC0012704 with the U.S. Department of Energy. The publisher by accepting the manuscript for publication acknowledges that the United States Government retains a non-exclusive, paid-up, irrevocable, world-wide license to publish or reproduce the published form of this manuscript, or allow others to do so, for United States Government purposes.

DISCLAIMER

This report was prepared as an account of work sponsored by an agency of the United States Government. Neither the United States Government nor any agency thereof, nor any of their employees, nor any of their contractors, subcontractors, or their employees, makes any warranty, express or implied, or assumes any legal liability or responsibility for the accuracy, completeness, or any third party's use or the results of such use of any information, apparatus, product, or process disclosed, or represents that its use would not infringe privately owned rights. Reference herein to any specific commercial product, process, or service by trade name, trademark, manufacturer, or otherwise, does not necessarily constitute or imply its endorsement, recommendation, or favoring by the United States Government or any agency thereof or its contractors or subcontractors. The views and opinions of authors expressed herein do not necessarily state or reflect those of the United States Government or any agency thereof.

Spatial interactions in hydrogenated perovskite nickelate synaptic networks

Ravindra Singh Bisht^{a,}, Jaeseoung Park^b, Haoming Yu^c, Chen Wu^d, Nikhil Tilak^e, Sylvie Rangan^e, Tae J. Park^c, Yifan Yuan^a, Sarmistha Das^d, Uday Goteti^d, Hee-Taek Yi^e, Hussein Hijazi^e, Abdullah Al-Mahboob^f, Jerzy T. Sadowski^f, Hua Zhou^g, Seongshik Oh^e, Eva Y. Andrei^e, Monica T. Allen^d, Duygu Kuzum^b, Alex Frano^d, Robert C. Dynes^d, and Shriram Ramanathan^{a,*}*

^aDepartment of Electrical and Computer Engineering, Rutgers University, Piscataway, NJ 08854, USA

^bDepartment of Electrical and Computer Engineering, University of California, San Diego, CA, USA

^cSchool of Materials Engineering, Purdue University, West Lafayette, IN, USA

^dDepartment of Physics, University of California, San Diego, CA 92093, USA

^eDepartment of Physics and Astronomy, Rutgers University, Piscataway, NJ 08854, USA

^fCenter for Functional Nanomaterials, Brookhaven National Laboratory, Upton, NY 11973, USA

^gX-ray Science Division, Advanced Photon Source, Argonne National Laboratory, Lemont, Illinois 60439, USA

Keywords. neuromorphic computing, perovskite nickelates, synaptic plasticity, quantum materials

Abstract

A key aspect of how the brain learns and enables decision-making processes is via synaptic interactions. Electrical transmission/communication in a network of synapses are modulated by extracellular fields generated by ionic chemical gradients. Emulating such spatial interactions in synthetic networks can be of potential use for neuromorphic learning and hardware implementation of artificial intelligence. Here, we demonstrate, in a network of hydrogen-doped perovskite nickelate devices, electric bias across a single junction can tune the coupling strength between the neighboring cells. Electrical transport measurements; spatially resolved diffraction and nano-probe X-ray and scanning microwave impedance spectroscopic studies suggest that graded proton distribution in the inhomogeneous medium of hydrogen-doped nickelate film enables this behavior. We further demonstrate signal integration through coupling of various junctions.

A principal goal of research in the field of neuromorphic computing is to emulate aspects of biological intelligence in hardware. Synapses in the brain are responsible for memory, learning, and in a broader sense control of the functioning of neural circuits.¹ This is accomplished in part by the ability of the synapses to modify their weight (referred to as plasticity) thereby modulating the firing of neuronal action potentials. Recent neuroscience studies have demonstrated synapses to be crucial for neural network regulation beyond simple plasticity.² In fact, the dynamic state of synapses has been noted as crucial for neural computation besides serving as memory storage.³ Synapses can control the flow of information either via chemical, electrical, or even a combination of both mechanisms (mixed synapses) as noted in studies on teleost fish.⁴ Extracellular fields generated by the ionic chemical potential gradients may enable synapses to control signal transmission in small-scale networks.⁵ That is, the coupling of neighboring neuronal cells can be

profoundly modified by individual synaptic action due to the local chemical disturbances occurring over characteristic neurotransmitter diffusional lengthscales, thereby affecting signal transmission in a neural circuit. It has been suggested that such coupling is important for establishing network function and complex spatiotemporal patterns of local field potentials in neuronal ensembles in various length scales.⁶⁻⁹ Gamma band activity and sharp-wave features are important for perception, learning, and memory in the brain.¹⁰⁻¹³ Function in large-scale neural networks require changes and control of membrane potentials of individual neurons which is achieved integration of incoming signals from a large number of neurons. Furthermore, neural networks such as those based on the Ising model¹⁴ shows that emergent computational phenomena such as categorization, associative memory^{15,16} are a consequence of interactions between network elements with wide-ranging spatial and temporal scales. Emulating the subtleties and complexity seen in various biological neural networks into artificial intelligence represents a frontier problem.¹⁷

Hydrogen donor doping of nickelates (e.g. NdNiO_3 (NNO)) has been shown to result in several orders of magnitude changes in electrical resistance at room temperature resulting from an e_g^2 half-filled configuration of the Ni d -orbitals upon electron injection.¹⁸ The magnitude of resistance change in a device can be controlled over several orders range by partial doping of the material utilizing forming gas annealing time-temperature envelopes. Protons reside in interstitial sites and can drift under electric fields. The extreme sensitivity of the electrical resistance of the nickelate to the concentration and distribution of protons in the lattice enables a wide range of resistance states that can be realized under pulsed voltage bias.^{19,20} Tuning resistance in individual hydrogen-doped nickelate devices under electric fields has been demonstrated previously, however understanding its impact in local networks is largely unknown. Here, we show that while potentiation, depression and learning rates of an individual synaptic device can be systematically

controlled by pulsed fields, the resistance of adjacent gap junctions can also be simultaneously modified due to the spatial drift of the protons. An electronically inhomogeneous medium comprising spatially varying proton concentrations enables this coupling and is verified by multi-modal scanning probe techniques (e.g. scattering and spectroscopy). At the same time, resistance tuning is limited to proximal nickelate junctions and hence promising to realize an artificial neurological substrate for brain-inspired electronics. Utilizing arrays of hydrogen-doped nickelate (H-NNO) devices, we then demonstrate signal integration through various junctions, an operation important for the integration of incoming signals that enable function of neural networks.

The synaptic junction is the space between two neuronal cells which controls electrical transmission/communication. The strengthening (potentiation) and weakening (depression) of the synaptic weight depends on the magnitude of the stimulus. The coupling between the different neuronal cells is depicted in **Figure 1a**. As shown, the stimulus applied to a single cell result in changing the coupling amongst the cells (shaded region with different gradients). In **Figure 1b**, we show the schematic (top and cross-sectional view) of the analogous H-NNO device study to illustrate the aforementioned concept. Each electrode represents a neuron node and the region between two electrodes represents a synapse. **Figure 1c** shows the band diagram of metallic NNO film at room temperature.²¹⁻²³ The hydrogen donor doping in the NNO leads to a change in the nominal nickel valence state from +3 to +2 due to electron filling in e_g orbitals and opens an electronic bandgap as schematically shown in **Figure 1d**. The protons upon hydrogenation couple weakly to the oxygen (**Figure 1d**) of the NNO lattice.²⁴ The ability to vary the spatial distribution of the protons and hence channel resistance, under an electric field is utilized for neuromorphic functionality.

In **Figure 2a**, the I-V characteristics of pristine NNO and H-NNO film are shown. As depicted, the resistance of H-NNO is greater than that of the NNO film (see **Figure S1** and supporting information for film growth, device fabrication, and electrical measurements). A significantly increased resistance for H-NNO in contrast to NNO film is attributed to the hydrogen doping that is controlled by the forming gas annealing conditions. The proton-electron doping in the NNO film leads to a large increase in the electronic bandgap due to carrier localization of doubly occupied e_g manifold by reducing Ni^{3+} sites to Ni^{2+} and therefore, a significant change in overall device resistance can be observed. To understand the device response to the polarity of an electric field, the electric field sweeps (50 cycles) for an asymmetric H-NNO device have been depicted in **Figures 2b** and **2c**. As observed, the resistance of the device increases with the application of a positive field sweep while it decreases with a negative field sweep. The electric field-driven modulation of resistance can be attributed due to the diffusion of interstitial protons in the H-NNO lattice. This also suggests that application of positive bias results in the expansion of the H-NNO region due to proton migration and vice versa. We then exploit this aspect to emulate the plasticity based on the H-NNO device i.e., mimicking the potentiation and depression process. To elucidate the plasticity, continuous electric pulses of magnitude 12 V and pulse width 100 μs were applied to increase the device resistance by nearly 25 $k\Omega$ and the device resistance was then reduced to nearly the original state by applying electric pulses of -10 V and 100 μs . Moreover, the rate of potentiation and depression can be tuned by magnitude of electric pulses as shown in **Figure 2d**. In **Figures 2e** and **2f**, we also show that the device resistance can be modulated to multiple resistance states and can be tuned back to the original resistive state. The resistance tuning mechanisms follow a power law and are non-linear,²⁵⁻²⁷ the non-linearity factor increases with an increase in pulse width (**Figure S2**). Representative retention and endurance data are shown in

Figure S3. The resistance switching mechanism for the H-NNO film describing the relationship between proton migration (that results in expansion of H-NNO region) and resistance modulation has been proposed in the literature^{20,28}. Using Einstein's relation $D = \frac{\mu K_B T}{q}$ and $v_d = \mu E$, the proton migration distance for the H-NNO device can be written as²⁹:

$$\Delta x = \frac{\Delta t * q * D * V}{K_B T L}, \text{ where } v_d = \frac{\Delta x}{\Delta t}.$$

$v_d, \mu, \Delta t, q, D, V, K_B, T, E$ and L represents the drift velocity, protons mobility, pulse width of a single electric bias stimulus, charge, diffusion constant, pulse voltage, Boltzmann constant, temperature, electric field, and width of the channel respectively. For $\Delta t = 100 \mu s, V = 12 \text{ V}$, and $L = 10 \mu m$ (one representative experimental condition used in our study), the estimated proton migration length is $\sim 0.40 \text{ nm}$ for a representative proton diffusion co-efficient of $8.7 \times 10^{-10} \text{ cm}^2/\text{s}$ (diffusion constant adapted from *reference 20*). It is likely the primary mechanism that modulates the resistance is the H-NNO/NNO interface proton distribution (due to the growth of the H-NNO region upon positive bias) and also noted from Kelvin force microscopy measurements of the electrode-HNNO interface before and after application of electric stimuli as described in a later section.

The spatial concentration of the local hydrogen ion distribution in H-NNO-based artificial synapse was modulated systematically by applying varying electrical pulses across one device junction and the resistance evolution across all the pairs of devices was studied. The optical image of the device studied is shown in **Figure S1**. Further, we demonstrate how this affects the properties of neighboring devices as shown in **Figure 2g**. A single positive electrical pulse of varying magnitude (E_i) was applied across electrodes 1 and 5, and resistance evolution ($\Delta R = R_f - R_i$) across other pairs of the electrode ($R_{12}, R_{13}, R_{14}, R_{15}, R_{23}, R_{24}, R_{25}, R_{34}, R_{35}$, and R_{45}) was measured. The R_i and

R_f represent the initial resistance of the junction and the resistance of the junction after pulsing. As shown, the electrodes that are in the vicinity of electrode 1, show a monotonic increase in the resistance, a behavior similar to the R_{15} . Importantly, this change in resistance or equivalently synaptic weight update for R_{12} , R_{13} , and R_{14} occurs without applying any additional electrical pulse across them. This increase in resistance at the adjacent junctions can be attributed to the change in the local proton distribution near electrode 1 upon electrical pulsing. The other pairs of devices (R_{23} , R_{24} , R_{25} , R_{34} , R_{35} , and R_{45}) do not show significant variation in the resistance. **Figure S4** further presents modulation of junction resistance across various pairs when an electric pulse was applied between electrodes 2 and 5 establishing general validity.

To understand how plasticity and synaptic coupling in H-NNO film can be utilized for biologically inspired computation, we then investigated signal integration through various junctions (See **Figure S5** and supporting information). Signal integration operation is similar to a weighted sum operation, widely used in artificial neural networks³⁰⁻³³.

To check the phase purity and structural evolution upon hydrogen doping in NNO film, the NNO and H-NNO films were characterized by synchrotron XRD using a micro-probe (see Supporting Information) as shown in **Figure 3a**. Due to a lattice mismatch between the film and substrate, the NNO film experiences an in-plane biaxial compressive strain. As a result, the out-of-plane lattice parameter, $c_{\text{NNO}} \sim 3.822 \text{ \AA}$, is larger than its bulk value of 3.807 \AA .²¹ Moreover, upon hydrogen doping the NNO peak further shifts to the lower L values, and the out-of-plane lattice parameter ($c_{\text{NNO}} \sim 3.836 \text{ \AA}$) shows a further elongation by $\sim 0.4 \%$. In **Figures S6a** and **S6b**, we also show the evolution of the doping profile between the Pd and Au electrodes for the device shown in **Figure S1**. As shown, the doping is dense near the Pd electrode and eventually fades toward the Au

electrodes. The micro XRD pattern of NNO and H-NNO films hence reveals an oriented (002) single-phase film grown on a LaAlO₃ substrate.

To measure the elemental composition of as well as hydrogen concentration in the nickelate films, we performed Rutherford backscattering spectroscopy (RBS) and elastic recoil detection analysis³⁴ (ERDA) (see Supporting Information). **Figures S7a** and **7b** show the RBS analysis of the NNO and H-NNO films. The NNO films are highly stoichiometric (**Table S1**). ERDA shows a clear increase in the hydrogen concentration in the doped films vs the undoped ones (**Figure 3b**). The ratio of the spatially averaged areal density of hydrogen to nickel estimated from experiments is 0.14 ($\frac{H}{Ni} \sim 0.14$), suggesting a partially doped H-NNO film. A similar increase in proton concentration ($\frac{H}{Ni} \sim 0.18$) has also been verified for a control sample independently prepared from electrochemically H-doped NNO film to verify the ERDA profile (**Figure S8**, and **Table S2**). The electronic structure of undoped and electrochemically doped films was also characterized using X-ray photoelectron spectroscopy XPS³⁵ (**Figure S9**) and indicates expected oxidation states and metallic vs semiconductor character (see Supporting Information).

We then utilize nanoscale X-ray absorption spectroscopy (XAS) to understand the proton distribution and change in the electronic structure near the Pd and Au electrodes (see Supporting Information). In **Figures 3c** and **3d**, we show the XAS analysis of the Ni *L*₃ edge of the NNO and H-NNO films. The multiplets were deconvoluted after a baseline subtraction and the spectra were fitted with two Gaussian components assigned for low energy (~856.3 eV) and high energy (~855.2 eV) peaks.^{36,37} As shown, the normalized integrated intensity for the low-energy peak (I₁) and high-energy peak (I₂) is enhanced (Orange) and suppressed (Blue) as a consequence of hydrogen doping and suggests a reduction in the Ni valence in H-NNO films near the Pd electrode. A full-range XAS scan of the Ni *L*_{2,3} edge for H-NNO film is depicted in **Figure 3e**. As shown, a

clear shift in the spectral weight of Ni $L_{2,3}$ edge to the lower energy, away from the Au electrode is attributed to a reduced Ni valence because of hydrogen doping near the catalytic Pd electrode. To understand the spatial variation and elucidate the extent of hydrogen doping in H-NNO films, spatially-resolved analysis of area ratio $\frac{I_2}{I_1}$ (Ni L_3 edge) was employed. It shows a heavily doped region of nearly 2 μm close to the Pd electrode (**Figure 3f**). In **Figure S10**, we also plot the $\frac{I_2}{I_1}$ as a function of distance from the Pd electrode. The spectral weight evolution of the low energy peak towards the Pd electrode thus confirms the dominant presence of Ni^{2+} near the Pd electrode. The spatially-resolved XAS analysis thus suggests a mixture of majority H-NNO regions and minority NNO regions in a solid matrix near the Pd electrode. Moreover, towards the Au electrode, the H-NNO regions are the minority in the solid matrix. Modulating these granular regions with electrical pulsing redistributes the protons and may lead to the observed electrical behavior (**Figure 2g**). Additionally, micro-diffraction mapping, X-ray photoemission electron microscopy (XPEEM),³⁸ and low-energy electron microscopy (LEEM) (see Supporting Information, **Figure 4a**, and **Figures S11**) shows a width of doped region consistent with the XAS study.

To understand the electronic phase transition upon hydrogen doping, we performed scanning Kelvin Probe Force Microscopy (KPFM)³⁹. In **Figures 4b** and **4c**, we depict a spatial map of the measured V_{CPD} for the NNO and H-NNO films, respectively. The areal extent of hydrogen doping for H-NNO film decays spatially due to the diffusive nature of doping (**Figure S12**). KPFM also shows a similar width of the doped region. Moreover, upon electrical pulsing, the Pd-NNO interface remains nearly unaffected while H-NNO/NNO shows changes (See supporting information, **Figure S13**, and **S14** showing KPFM data). This further suggests the mechanism of change in resistance upon electrical pulsing is primarily due to proton migration.

While the spectroscopy and microscopy techniques utilized above give detailed information on the electronic structure/surface potential, a local conductivity map over a large region can provide additional evidence of the inhomogeneous doping which leads to the phase coexistence of NNO and H-NNO regions in a solid matrix. To acquire a conductivity map, we employed microwave impedance microscopy (MIM) (see Supporting Information and **Figure S15**) to image the conductivity contrast across the interface of the NNO and H-NNO region. The scan area, represented by the red box in **Figure S16**, encloses both the H-NNO and pristine NNO regions. Our measurements reveal that local changes in conductivity are spatially correlated with the real-space distribution of hydrogen doping. The technique of MIM probes the electronic properties of materials by measuring the complex tip-sample admittance, which depends on the local permittivity and conductivity of the sample. The theoretical real and imaginary parts of the MIM response (MIM-Re and MIM-Im, respectively) are plotted in **Figure 4d** and are obtained from finite element simulations of the experimental MIM setup at 155 MHz. At room temperature, prior experiments have reported that pristine NNO should have a resistivity of $10^{-5} \Omega\text{m}$.⁴⁰ For comparison, the transport results reported in this work indicate that H-NNO should have a resistivity of nearly $\sim 10^3$ - 10^4 larger than the NNO. Therefore, based on the response curves in **Figure 4d**, it is expected that the resistive H-NNO region should yield a MIM-Im signal saturated near zero, while the conductive NNO region should have a finite MIM-Im signal that is saturated at the other end in the response curve. We should therefore see a clear MIM contrast between these two regions. The two panels (a) and (b) in **Figure S17** display MIM-Im and MIM-Re images obtained near the boundary between the NNO and H-NNO regions, where the color change reflects the change in conductivity with the position. Right outside of the H-NNO region, non-uniform spatial features appear to penetrate from the H-NNO region (**Figure S17c**). These spatial

inhomogeneities of the local conductivity are more visible in the detailed scans of the interface in **Figure 4e**. **Figures 4f** and **S17c** display the relative phase of the dC/dV signal, which can shed light on the type of charge carrier.⁴¹ The H-NNO region shows a higher phase value relative to the pristine NNO region (**Figure 4f**), corresponding to the electrons that the hydrogen atoms donate.

In summary, multi-modal spectroscopic characterization reveals that an electronically inhomogeneous nickelate medium due to graded hydrogen doping can serve as a platform for tuning electrical resistance upon voltage application. Future studies exploring different electrode geometries and network patterns could serve to examine the evolution of weights in more complex networks. Quantum materials whose electronic properties can be tuned by ion doping offer an interesting platform to examine neuromorphic functions.

ASSOCIATED CONTENT

Details on experimental methods; weighted sum measurements; structural characterization of NNO thin films; optical image of the device used (**S1**); non-linearity analysis of potentiation and depression curves (**S2**); device stability and electrical characterization of H-NNO network (**S3-S4**); weighted sum measurements (**S5**); detailed structural characterizations (**S6-S17**, **Table S1**, and **S2**).

AUTHOR INFORMATION

Corresponding Authors

Ravindra Singh Bisht- *Department of Electrical and Computer Engineering, Rutgers University, Piscataway, NJ 08854, United States; Email: ravindra.bisht@rutgers.edu*

Shriram Ramanathan- *Department of Electrical and Computer Engineering, Rutgers University, Piscataway, NJ 08854, United States; Email: shriram.ramanathan@rutgers.edu*

Authors

Jaeseoung Park- *Department of Electrical and Computer Engineering, University of California, San Diego, CA, United States*

Haoming Yu- *School of Materials Engineering, Purdue University, West Lafayette, IN, United States*

Chen Wu- *Department of Physics, University of California, San Diego, CA 92093, United States,*

Nikhil Tilak- *Department of Physics and Astronomy, Rutgers University, Piscataway, NJ 08854, United States*

Sylvie Rangan- *Department of Physics and Astronomy, Rutgers University, Piscataway, NJ 08854, United States*

Tae Joon Park- *School of Materials Engineering, Purdue University, West Lafayette, IN, United States*

Yifan Yuan- *Department of Electrical and Computer Engineering, Rutgers University, Piscataway, NJ 08854, United States*

Sarmistha Das- *Department of Physics, University of California, San Diego, CA 92093, United States*

Uday Goteti- *Department of Physics, University of California, San Diego, CA 92093, United States*

Hee-Taek Yi- *Department of Physics and Astronomy, Rutgers University, Piscataway, NJ 08854, United States*

Hussein Hijazi- *Department of Physics and Astronomy, Rutgers University, Piscataway, NJ 08854, United States*

Abdullah Al-Mahboob- *Center for Functional Nanomaterials, Brookhaven National Laboratory, Upton, NY 11973, United States*

Jerzy T. Sadowski- *Center for Functional Nanomaterials, Brookhaven National Laboratory, Upton, NY 11973, United States*

Hua Zhou- *X-ray Science Division, Advanced Photon Source, Argonne National Laboratory, Lemont, Illinois 60439 USA*

Seongshik Oh- *Department of Physics and Astronomy, Rutgers University, Piscataway, NJ 08854, United States*

Eva Y. Andrei- *Department of Physics and Astronomy, Rutgers University, Piscataway, NJ 08854, United States*

Monica T. Allen- *Department of Physics, University of California, San Diego, CA 92093, USA*

Duygu Kuzum- *Department of Electrical and Computer Engineering, University of California, San Diego, CA, United States*

Alex Frano- *Department of Physics, University of California, San Diego, CA 92093, United States*

Robert C. Dynes- *Department of Physics, University of California, San Diego, CA 92093, United States*

Author Contributions

RSB, JP, DK, AF, RCD, and SR designed the study. RSB, JP, HY, CW, NT, Sylvie Rangan, and SD performed the research; RSB and HY grew the samples and fabricated the devices. RSB and JP performed electrical measurements. Sylvie Rangan performed XPS and valence Band

measurements. RSB and HTY performed catalytic hydrogen doping using a furnace setup by SO. TJP performed hydrogen doping electrochemically. CW and MTA performed MIM measurements. HH performed RBS and ERDA measurements. NT and RSB performed KPFM measurements and analysis. HZ performed synchrotron micron-XRD measurements. AM and JS performed XAS, XPEEM, and LEEM measurements. RSB and JP analyzed the data. RSB, JP, DK, and SR wrote the paper with input from all the authors. All the authors discussed the results.

Notes

The authors declare no competing financial interest.

ACKNOWLEDGMENTS

The network concept development and electrical measurements were funded by “Quantum Materials for Energy Efficient Neuromorphic Computing”, an Energy Frontier Research Center funded by the U.S. Department of Energy (DOE), Office of Science, Basic Energy Sciences. This research used resources of the Center for Functional Nanomaterials and the National Synchrotron Light Source II, which are U.S. Department of Energy (DOE) Office of Science facilities at Brookhaven National Laboratory, under Contract No. DE-SC0012704. This research used resources of the Advanced Photon Source, a U.S. Department of Energy (DOE) Office of Science user facility at Argonne National Laboratory, and is based on research supported by the U.S. DOE Office of Science-Basic Energy Sciences, under Contract No. DE-AC02-06CH11357. We acknowledge AFOSR grant FA9550-22-1-0344 that supported the ion beam scattering characterization of the films. HTY and SO are supported by National Science Foundation’s DMR2004125 and the Center for Quantum Materials Synthesis (cQMS), funded by the Gordon and Betty Moore Foundation’s EPiQS initiative through Grant GBMF10104. The authors acknowledge the Laboratory for Surface Modification Facilities at Rutgers University for XPS,

ERDA, and RBS measurements. NT and EYA acknowledge Gordon and Betty Moore Foundation EPIQS initiative GBMF9453 and Department of Energy DOE-FG02-99ER45742 for support. RSB, YY, and SR gratefully thank Kevin Wine at Rutgers University for helping set up the probe station. RSB and SR thank Professor Leonard C. Feldman from Rutgers University for an insightful discussion on ion beam analysis. SR thanks Professor Alberto E. Pereda from the Albert Einstein College of Medicine for valuable discussions on synapses in teleost fish.

REFERENCES

1. Abbott, L. F.; Nelson, S. B. Synaptic plasticity: taming the beast. *Nat. Neurosci.* **2000**, *3*, 1178-1183.
2. Alcamí, P.; Pereda, A. E. Beyond plasticity: the dynamic impact of electrical synapses on neural circuits. *Nat. Rev. Neurosci.* **2019**, *20*, 253-271.
3. Abbott, L. F.; Regehr, W. G. Synaptic computation. *Nature* **2004**, *431*, 796-803.
4. Pereda, A. E. Electrical synapses and their functional interactions with chemical synapses. *Nat. Rev. Neurosci.* **2014**, *15*, 250-263.
5. Faber, D. S.; Pereda, A. E. Two forms of electrical transmission between neurons. *Front. Mol. Neurosci.* **2018**, *11*, 427.
6. Traub, R.D.; Kopell, N.; Bibbig A.; Buhl, E. H., LeBeau, F.E.; Whittington, M. A. Gap junctions between interneuron dendrites can enhance synchrony of gamma oscillations in distributed networks. *J. Neurosci.* **2001**, *21(23)*, 9478-86.
7. Pernelle, G.; Nicola, W.; Clopath, C. Gap junction plasticity as a mechanism to regulate network-wide oscillations. *PLoS Comput. Biol.* **2018**, *14(3)*, e1006025.

8. Traub, R. D.; Schmitz, D.; Jefferys, J. G.; Draguhn, A. High-frequency population oscillations are predicted to occur in hippocampal pyramidal neuronal networks interconnected by axoaxonal gap junctions. *Neurosci.* **1999**, *92(2)*, 407-26.
9. LeBeau, F. E.; Traub, R. D.; Monyer, H.; Whittington, M. A.; Buhl, E. H. The role of electrical signaling via gap junctions in the generation of fast network oscillations. *Brain Res. Bull.* **2003**, *62(1)*, 3-13.
10. Bragin, A.; Engel, Jr. J.; Wilson, C. L.; Fried, I.; Buzsáki, G. High-frequency oscillations in human brain. *Hippocampus.* **1999**, *9(2)*, 137-42.
11. Buzsaki, G.; Draguhn, A. Neuronal oscillations in cortical networks. *Science.* **2004**, *304(5679)*, 1926-1929.
12. Canakci, S.; Toy, M. F.; Inci, A. F.; Liu, X.; Kuzum, D. Computational analysis of network activity and spatial reach of sharp wave-ripples. *PLOS ONE.* **2017**, *12(9)*, e0184542.
13. Buzsaki, G. *Rhythms of the Brain.* Oxford university press, **2006**.
14. Hopfield, J. J. Neural networks and physical systems with emergent collective computational abilities. *Proc. Natl. Acad. Sci. U.S.A.* **1982**, *79*, 2554-2558.
15. Amit, D. J.; Gutfreund, H.; Sompolinsky, H. Spin-glass models of neural networks. *Phys. Rev. A* **1985**, *32*, 1007.
16. Peretto, P. Collective properties of neural networks: a statistical physics approach. *Biol. Cybern.* **1984**, *50*, 51-62.
17. Goteti, U. S.; Zaluzhnyy, I. A.; Ramanathan, S.; Dynes, R.C.; Frano, A. Low-temperature emergent neuromorphic networks with correlated oxide devices. *Proc. Natl. Acad. Sci. U.S.A.*, **2021**, *118*, 35.

18. Shi, J.; Zhou, Y.; Ramanathan, S. Colossal resistance switching and band gap modulation in a perovskite nickelate by electron doping. *Nat. Commun.* **2014**, *5*, 1-9.
19. Oh, C.; Heo, S.; Jang, H. M.; Son, J. Correlated memory resistor in epitaxial NdNiO₃ heterostructures with asymmetrical proton concentration. *Appl. Phys. Lett.* **2016**, *108*, 122106.
20. Sidik, U.; Hattori, A. N.; Rakshit, R.; Ramanathan, S.; Tanaka, H. Catalytic hydrogen doping of NdNiO₃ thin films under electric fields. *ACS Appl. Mater. Interfaces.* **2020**, *12* (49), 54955-54962.
21. Catalan, G. Progress in perovskite nickelate research. *Phase Transit.* **2008**, *81*, 729-749.
22. Catalano, S.; Gibert, M.; Fowlie, J.; Iniguez, J.; Triscone, J.- M.; Kreisel, J. Rare-earth nickelates RNiO₃: thin films and heterostructures. *Rep. Prog. Phys.* **2018**, *81*, 046501.
23. Middey, S.; Chakhalian, J.; Mahadevan, P.; Freeland, J.W.; Millis, A.J.; Sarma, D.D. Physics of ultrathin films and heterostructures of rare-earth nickelates. *Annu. Rev. Mater. Res.* **2016**, *46*, 305-334.
24. Zhou, Y.; Guan, X.; Zhou, H.; Ramadoss, K.; Adam, S.; Liu, H.; Lee, S.; Shi, J.; Tsuchiya, M.; Fong, D. D.; Ramanathan, S. Strongly correlated perovskite fuel cells. *Nature* **2016**, *534*, 231-234.
25. Tang, J.; He, C.; Tang, J.; Yue, K.; Zhang, Q.; Liu, Y.; Wang, Q.; Wang, S.; Li, N.; Shen, C.; Zhao, Y. A reliable all-2D materials artificial synapse for high energy-efficient neuromorphic computing. *Adv. Funct. Mater.* **2021**, *31*, 2011083.
26. Chen, P.Y.; Lin, B.; Wang, I.T.; Hou, T.H.; Ye, J.; Vruthula, S.; Seo, J.S.; Cao, Y.; Yu, S. Mitigating effects of non-ideal synaptic device characteristics for on-chip learning.

- IEEE/ACM International Conference on Computer-Aided Design (ICCAD)*. **2015**, pp.194-199.
27. Tang, J.; Bishop, D.; Kim, S.; Copel, M.; Gokmen, T.; Todorov, T.; Shin, S.; Lee, K.T.; Solomon, P.; Chan, K.; Haensch, W. ECRAM as scalable synaptic cell for high-speed, low-power neuromorphic computing. *IEEE International Electron Devices Meeting (IEDM)*. **2018**, pp. 13-1.
 28. Sidik, U.; Hattori, A. N.; Hattori, K.; Alaydrus, M.; Hamada, I.; Pamasi, L. N.; Tanaka, H. *ACS Appl. Electron. Mater.* **2022** 4 (10), 4849-4856.
 29. Sidik, U., Hattori, A. N., Li, H. B., Nonaka, S., Osaka, A. I., Tanaka, H. *Appl. Phys. Express*. **2023**, 16, 014001.
 30. He, K.; Zhang, X.; Ren, S.; Sun, J. Deep Residual Learning for Image Recognition. *Proceedings of the IEEE Conference on Computer Vision and Pattern Recognition*. **2016**, 770-778.
 31. Krizhevsky, A.; Sutskever, I.; Hinton, G. E. Imagenet classification with deep convolutional neural networks. *Commun. ACM* **2017**, 60, 84-90.
 32. Vaswani, A.; Shazeer, N.; Parmar, N.; Uszkoreit, J.; Jones, L.; Gomez, A. N.; Kaiser, Ł.; Polosukhin, I. Attention is all you need. *Advances in Neural Information Processing Systems* **2017**, 30.
 33. Oh, S.; Shi, Y.; Del Valle, J.; Salev, P.; Lu, Y.; Huang, Z.; Kalcheim, Y.; Schuller, I. K.; Kuzum, D. Energy-efficient Mott activation neuron for full-hardware implementation of neural networks. *Nat. Nanotechnol.* **2021**, 16, 680-687.
 34. Feldman, L. C.; Mayer, J. W. *Fundamentals of surface and thin film analysis* (New York : North-Holland, **1986**).

35. Amarasinghe, D. K.; Yu, H.; Rodolakis, F.; Zhou, H.; Cao, H.; Ramanathan, S., Electron doping of NdNiO₃ thin films using dual chamber CaH₂ annealing. *J. Solid State Chem.* **2022**, *315*, 123512.
36. Medarde, M.; Fontaine, A.; García-Muñoz, J.L.; Rodríguez-Carvajal, J.; De Santis, M.; Sacchi, M.; Rossi, G.; Lacorre, P. RNiO₃ perovskites (R= Pr, Nd): Nickel valence and the metal-insulator transition investigated by x-ray-absorption spectroscopy. *Phys. Rev. B* **1992**, *46*, 14975.
37. Freeland, J. W.; Veenendaal, M. V.; Chakhalian, J. Evolution of electronic structure across the rare-earth RNiO₃ series." *J. Electron Spectrosc. Relat. Phenom.* **2016**, *208*, 56-62.
38. Li, J.; Green, R.J.; Zhang, Z.; Sutarto, R.; Sadowski, J.T.; Zhu, Z.; Zhang, G.; Zhou, D.; Sun, Y.; He, F.; Ramanathan, S.; Comin., R. Sudden collapse of magnetic order in oxygen-deficient nickelate films. *Phys. Rev. Lett.* **2021**, *126*, 187602.
39. Melitz, W.; Shen, J.; Kummel, A. C.; Lee, S. Kelvin probe force microscopy and its application. *Surf. Sci. Rep.* **2011**, *66*, 1-27.
40. Preziosi, D.; Lopez-Mir, L.; Li, X.; Cornelissen, T.; Lee, J.H.; Trier, F.; Bouzehouane, K.; Valencia, S.; Gloter, A.; Barthélémy, A.; Bibes, M. Direct mapping of phase separation across the metal–insulator transition of NdNiO₃, *Nano Lett.* **2018**, *18*, 2226.
41. Kundhikanjana, W.; Yang, Y.; Tanga, Q.; Zhang, K.; Lai, K.; Ma, Y.; Kelly, M. A.; Li, X. X.; Shen, Z. X. Unexpected surface implanted layer in static random access memory devices observed by microwave impedance microscope, *Semicond. Sci. Technol.* **2013**, *28*, 025010.

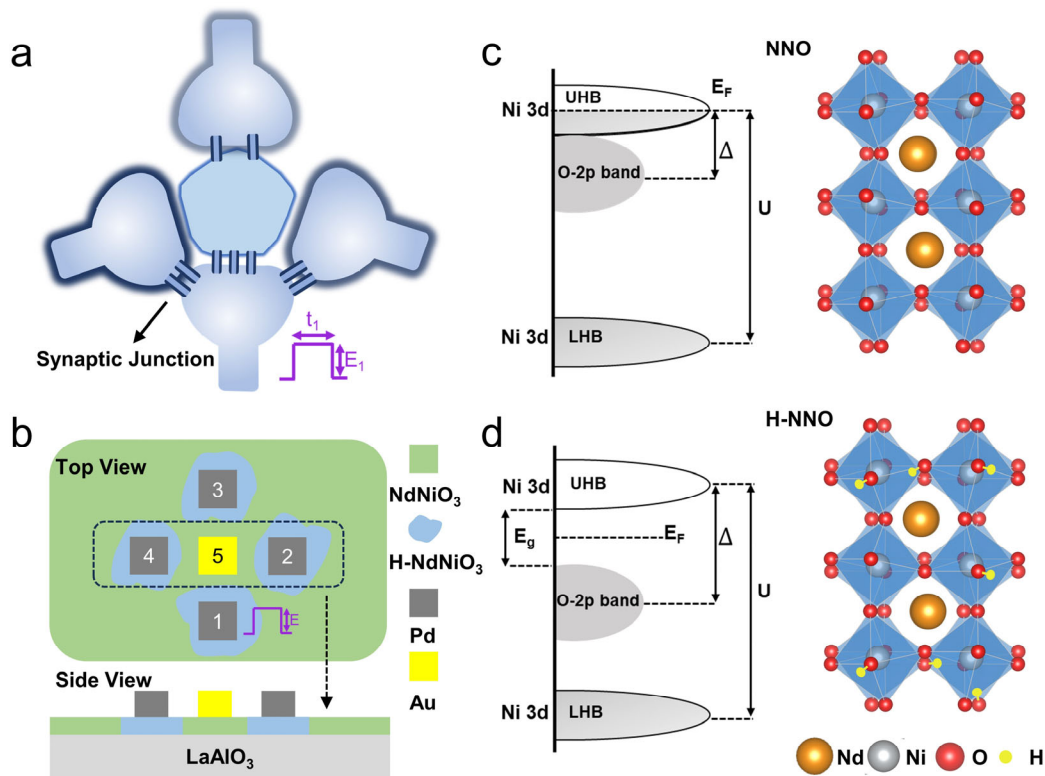


Figure 1. Schematic illustration of coupling between neuronal cells and electronic analog in NdNiO₃. (a) Extracellular field coupling amongst different neuronal cells in a biological synaptic network. The coupling between neighboring cells can be tuned by synaptic action across one junction. The different shades of color illustrate different coupling strengths. Each cell represents a neuron and the lines connecting the cells represent synaptic junction. (b) Schematic (top and cross-sectional view) of in-plane NNO device with Pd and Au electrodes. The Pd electrodes serve as a catalyst for hydrogen doping of the NNO film with heavier doping proximal to the Pd electrode. The graded concentration of the dopants across the electrode junctions can be modulated by electric bias. The synaptic action across electrode 1 leads to a change in the coupling strength with nearby electrodes. The heavily doped region is shown in blue color as a visual guide. (c)

Schematic of band diagram and structure of perovskite NNO at room temperature. (d) The hydrogen doping leads to a reduction in Ni valence from +3 to +2 and as a result of electronic correlation, a band gap opens up. The protons diffused in the NNO lattice are weakly coupled to the oxygen atom of Ni-O octahedra. The E_g , E_F , U and Δ represents the electronic bandgap, Fermi energy, on-site coulomb repulsion, and charge transfer energy respectively.

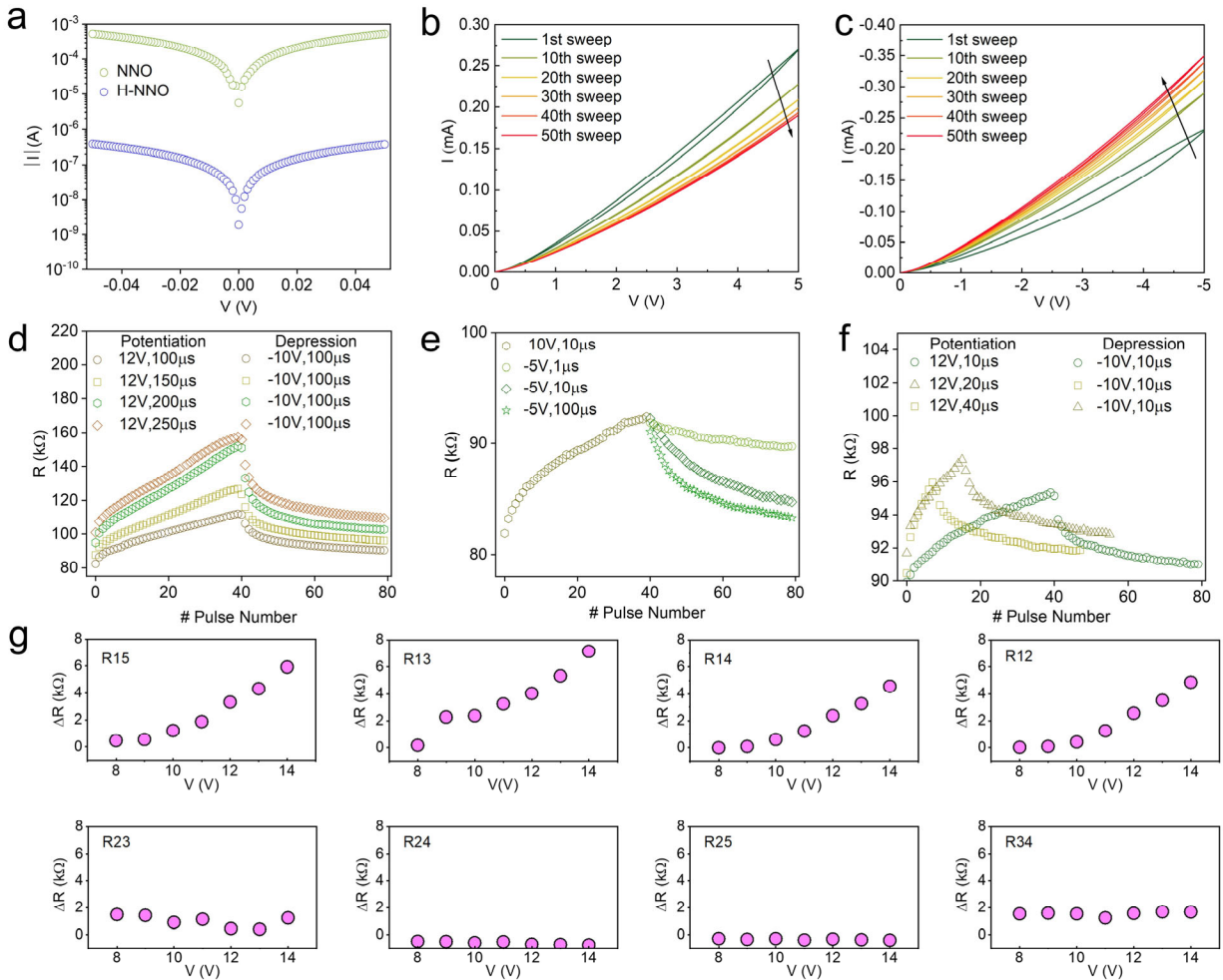


Figure 2. Demonstration of plasticity in H-NNO thin film device and the emergence of coupling and resistance evolution. (a) I-V characteristics of NNO and H-NNO films. A several-order-of-magnitude change in the resistance of H-NNO film compared to the NNO film indicates carrier localization upon electron doping. (b), (c) The I-V characteristics (shown for every 10th cycle)

under a positive and negative voltage sweep show a continuous increase and decrease in the resistance of the H-NNO device respectively. The modulation of device resistance depends on the spatial drift of interstitial protons in the presence of an electric field. (d) The potentiation and depression curves for the H-NNO device. Different stimuli were used for the potentiation while keeping the stimulus the same during the depression. Tuning the device resistance to different states by changing the stimuli for (e) depression and (f) potentiation. In both cases, a constant ΔR was maintained. (g) An electric pulse E_i of varying magnitude and pulse width $100 \mu\text{s}$ is applied across electrodes 1 and 5, and a change in resistance $\Delta R = R_f - R_i$ across various pairs of electrodes is shown. The electric pulse modulates the proton distribution near electrode 1 and hence affects the resistance of adjacent electrodes (R_{12} , R_{13} , R_{14}) in the vicinity of electrode 1. An increase in the R_{13} could likely be attributed due to a current flow from electrode 1 to electrode 5 and electrode 5 to electrode 3. Therefore, a combination of R_{15} and R_{35} might be responsible for a slightly larger effect than that of R_{15} or R_{12}/R_{14} .

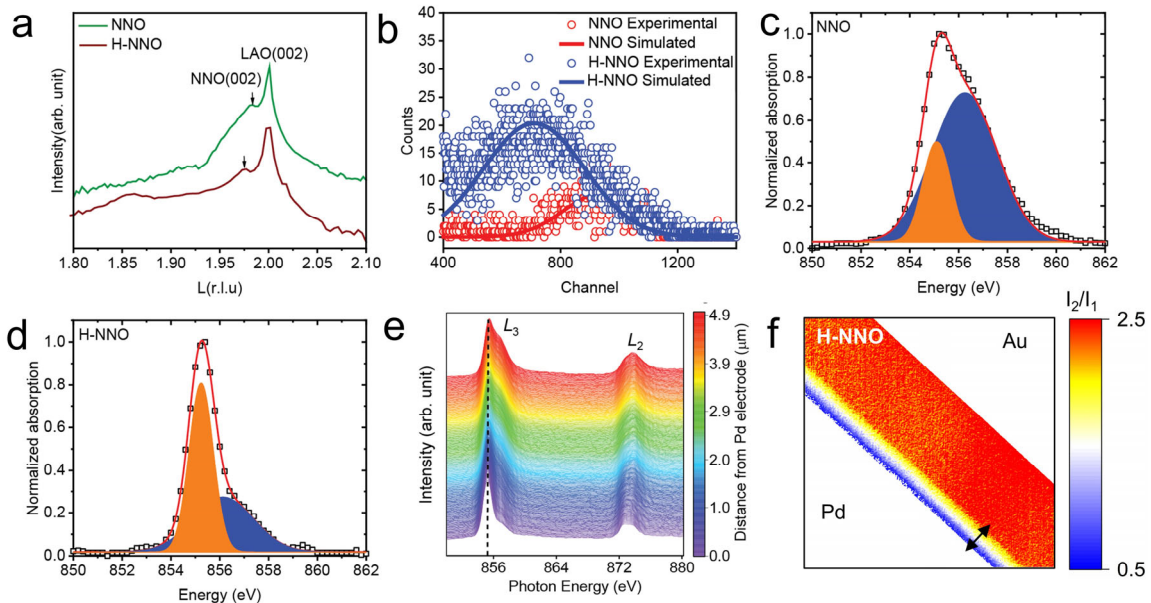


Figure 3. Structural and electronic structure characterization of H-NNO films. (a) The synchrotron micro XRD pattern of NNO and H-NNO films. The reciprocal lattice unit (r.l.u.) was defined using the lattice parameter ($a_{pc} \sim 3.79 \text{ \AA}$) of the LAO (001) substrate. The arrow marks the peak position of NNO before and after hydrogen doping. (b) ERDA analysis for pristine NNO and H-NNO film showing an increase in hydrogen content for H-NNO film. The solid lines in each curve represent the corresponding simulated spectrum. An offset in channel number for H-NNO is due to a Pt film on top used for hydrogenation. (c), (d) The deconvoluted normalized XAS Ni L_3 edge spectra of NNO and H-NNO films. (e) A full range XAS spectra of H-NNO film as a function of distance from the Pd edge. The dashed line marks the shift in peak positions. (f) Spatially resolved area ratio $\frac{I_2}{I_1}$ of the Ni L_3 spectra of H-NNO film. The arrow marks the width ($\sim 2\mu\text{m}$) of the doped region near the Pd electrode.

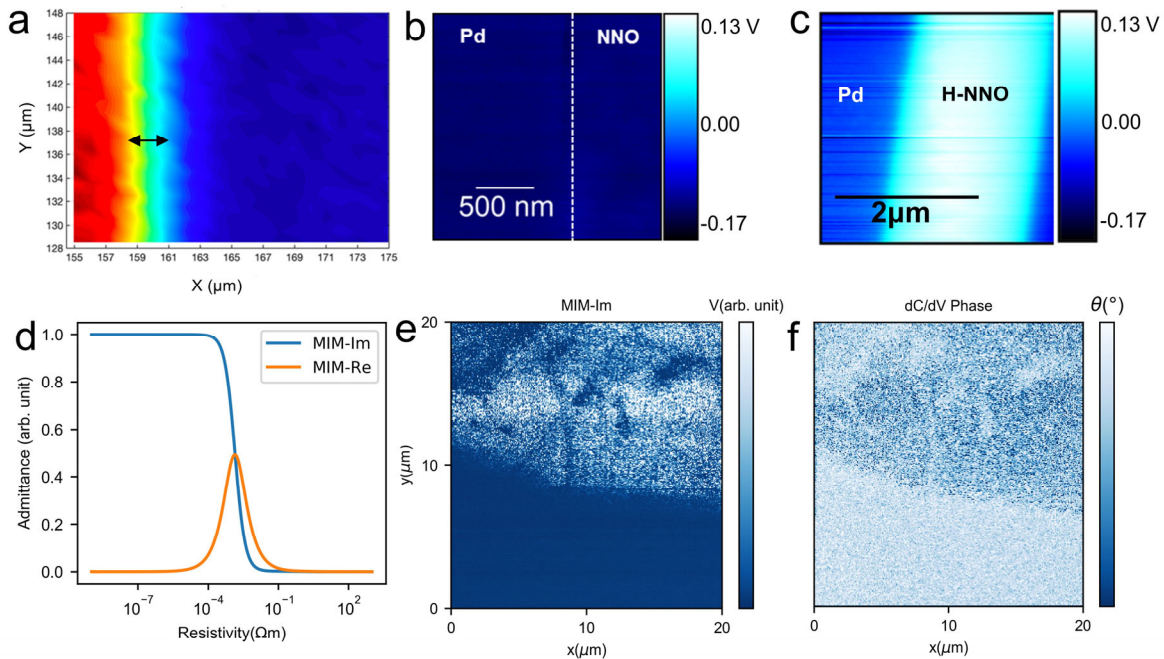


Figure 4. Spatial characterization of H-NNO films. (a) Micro-diffraction 2D mapping of H-NNO film intensity ($L = 1.85$) demonstrates the extended width of hydrogen doped region away from

the edge of Pd. The arrow marks the width ($\sim 2\mu\text{m}$) of the doped region. KPFM contact potential difference map of the asymmetric (b) NNO and (c) H-NNO device. The dashed line in (b) represents the boundary between the Pd electrode and the NNO film. A distinct difference in the contact potential difference profile for H-NNO device is attributed due to hydrogen doping. A contrast in the contact potential difference near the Pd electrode for H-NNO film represents the areal extent of the hydrogen doping. The estimated width of the doped region is in good agreement with the Micron diffraction mapping, LEEM, and XPEEM imaging. (d) Theoretical MIM response curves, simulated using finite-element analysis at 155 MHz, show how the reflected MIM signal depends on the local resistivity of the sample. A small-area scan in the immediate vicinity of the boundary between the H-NNO and NNO areas. (e) The imaginary MIM channel, and (f) the relative phase of the dC/dV -mode image.